Local Energy Landscape Drives Long-Range Exciton Diffusion in Two-Dimensional Halide Perovskite Semiconductors

Alan Baldwin [a,b §], Géraud Delport [a, §,†], Kai Leng [c], Rosemonde Chahbazian [a], Krzysztof Galkowski [a,e], Kian Ping Loh [d] and Samuel D. Stranks [a,b]*

a) Alan Baldwin, Dr. Géraud Delport, Rosemonde Chahbazian, Dr. Krzysztof Galkowski and Dr. Samuel D. Stranks
Cavendish Laboratory, University of Cambridge, JJ Thomson Avenue, Cambridge CB3 0HE, UK.

b) Alan Baldwin, Dr. Samuel D. Stranks
Department of Chemical Engineering & Biotechnology, University of Cambridge, Philippa Fawcett Drive, Cambridge CB3 0AS, UK

c) Dr. Kai Leng
Department of Applied Physics, The Hong Kong Polytechnic University, Hung Hom, Kowloon, Hong Kong, China.

d) Prof. Kian Ping Loh
Department of Chemistry, National University of Singapore, Singapore, Singapore.

e) Dr. Krzysztof Galkowski
Institute of Physics, Faculty of Physics, Astronomy and Informatics, Nicolaus Copernicus University, 5th Grudziadzka St., 87−100 Toruń, Poland

AUTHOR INFORMATION

* Corresponding Author : Dr. Samuel D. Stranks E-mail: sds65@cam.ac.uk

Abstract:

Halide perovskites are versatile semiconductors with applications including photovoltaics and light emitting devices, having modular optoelectronic properties realisable through composition and dimensionality tuning. Layered Ruddlesden-Popper perovskites are particularly interesting due to their unique two-dimensional character and charge carrier dynamics. However, long-range energy transport through exciton diffusion in these materials is not understood or realised. Here, local time-resolved luminescence mapping techniques are employed to visualize exciton transport in exfoliated flakes of the $BA_2MA_{n-1}Pb_nI_{3n+1}$ perovskite family. Two distinct transport regimes are uncovered, depending on the temperature range. Above 100 K, diffusion is mediated by thermally activated hopping processes between localised states. At lower temperatures, a non-uniform energetic landscape emerges in which transport is dominated by downhill energy transfer to lower energy states, leading to long-range transport over hundreds of nanometres. Efficient, long-range, and switchable downhill transfer offers exciting possibilities of controlled directional long-range transport in these 2D materials for new applications.

TOC GRAPHICS

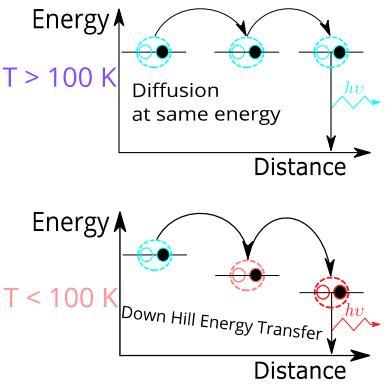

KEYWORDS Halide Perovskites, 2D semiconductors, exciton diffusion, exciton-phonon coupling, trapping

Halide perovskites have emerged as disruptive semiconductors for applications including photovoltaics and light emitting devices, with modular optoelectronic properties realisable through composition and dimensionality tuning. Layered Ruddlesden-Popper perovskites of the form $BA_2MA_{n-1}Pb_nI_{3n+1}$, where *n* is the number of lead-halide and methylammonium (MA) sheets spaced by longer butylammonium (BA) cations, are particularly interesting due to their unique two-dimensional character and charge carrier dynamics dominated by strongly bound excitons. However, long-range energy transport through exciton diffusion in these materials is not understood or realised. Here, local time-resolved luminescence mapping techniques are employed to visualize exciton transport in high-quality exfoliated flakes of the $BA_2MA_{n-1}Pb_nI_{3n+1}$ perovskite family. Two distinct transport regimes are uncovered, depending on the temperature range studied. At temperatures above 100 K, diffusion is mediated by thermally activated hopping processes between localised states. At lower temperatures, a non-uniform energetic landscape emerges in which exciton transport is dominated by downhill energy transfer to lower energy states, leading to long-range transport over hundreds of nanometres even in the absence of exciton-phonon coupling and in the presence of local optoelectronic heterogeneity. Efficient, long-range, and switchable downhill excitonic transfer offers exciting possibilities of controlled directional long-range transport in these 2D materials for new device applications.

Halide perovskites have intrigued the semiconductor community for the last decade, challenging the established understanding that defect concentrations in semiconductors must be minimised at all costs for high device performance[1], which typically requires complex fabrication methods.

Remarkably, the perovskite structure offers the possibility to tune the crystal dimensionality and the inherent photophysical properties, for example by changing the length and nature of the A-site cation out of a large library of compatible molecules[2]. Ruddlesden-Popper perovskites (RPPs) hold a special place in the perovskite family due to their unique two dimensional character (Figure 1a) and their enhanced stability with respect to conventional 3D perovskites to atmosphere and under illumination[3,4]. These materials take the general formula $S_2A_{n-1}B_nX_{3n+1}$ where S represents a large organic spacer cation, A is a small monovalent cation, B a divalent metal and X a halide anion. Structurally, they are composed of corner-sharing BX_6 octahedra quasi-2D layers, with n representing the number of BX_6 planes, with the layers separated by bulky S molecules[5–7]. High-quality single crystal RPPs can be fabricated and mechanically exfoliated to yield any desired number of layers[6,8], paving the way for ultrathin optoelectronic devices[9]. The two-dimensionality of each of the layers coupled with the low dielectric constant of the spacer molecules results in charge dynamics which are dominated by strongly bound excitons[5,10–12]. The remarkable photophysical properties of these RPPs have been utilised in various domains such as lasers[13], LEDs[14] and in efficient, stable perovskite solar cells[15]. In particular, long lived and highly diffusive excitons can be generated in such RPPs, while their emission spectra can be greatly modified due to local low energy states[16] or the presence of n RPP domains[17] within the same sample. The study of the charge carrier diffusion in such RPPs is a complex but essential one, for ultimately attaining fine control over energy transport in these materials and associated devices. In this context, recent studies have started to disentangle the influence of photon recycling[18], phonons[19], or shallow traps states[20], paving the way toward a better understanding of the global charge carrier transport mechanism in such RPPs. Nevertheless, many aspects related to the exciton

recombination and transport, particularly on the local scale, how local physicochemical properties impact these phenomena, remain to be investigated.

Here, we employ time-resolved photoluminescence microscopy[21–23] (TRPL), coupled to a helium cryostat, to visualise the local charge carrier dynamics and diffusion properties as a function of temperature in $BA_2MA_{n-1}Pb_nI_{3n+1}$ (BA = butylammonium, MA = methylammonium) flakes (see SI Sections I - IV and Figure S1 for a description of the customised confocal photoluminescence setup). We focus on the $n = 4$ system, with similar results obtained for $n = 2$, with the flakes having been exfoliated from macroscopic single crystals. The exciton binding energy in such $n = 4$ (or $n = 2$) perovskites is on the order of hundreds of millielectron volts[10], implying that the carriers form a majority of excitons in all but one of the experimental conditions used in our study (see SI Section V and Figure S2 for details). For temperatures in the range 300 – 100 K, we observe diffusive transport in which exciton-phonon coupling plays a crucial role resulting in a thermally activated hopping process through localised states, which are also responsible for the non-radiative decay of these excitons. At temperatures below 100 K, such hopping processes become inefficient and local energy gradients take precedence over exciton-phonon coupling, leading to a transport regime driven by local energy gradients across a varying bandgap landscape originating from local phase or structural variations. Such energy gradients lead to exciton transport on length scales of up to 600 nm (see SI Section VI) associated with strong luminescence from low energy sites in the flakes. This study reveals that long-range directional energy transport is possible if local energetic landscapes can be controlled and exploited, paving the way towards new devices based on 2D materials including transistors, light emitting devices and photodetectors.

We focus our study on the exciton dynamics in $n = 4$ exfoliated thin RPP crystals deposited on a silicon substrate and encapsulated with a hexagonal Boron-Nitride (h-BN) layer to ensure

environmental and illumination stability[9] (see SI Section I for details and Figure 1a for schematic structure of $n = 4$ sample). We also observe similar results to those reported here for $n = 2$ crystals (SI Section XIII). An optical image of one of the flakes of interest is shown in Figure 1b with a thickness of ≈ 9 stacked quantum wells (≈ 30 nm thickness), based on the optical contrast[6] of the flake and on previous studies[9] (see SI Section VII and Figure S3 for details), with PL (Figure 1d) and XRD (SI Section VIII, Figures S4 and Table S1) measurements suggesting that the flakes are highly phase pure. Such thin flakes maximize our chances to accurately separate the exciton diffusion process from other physical effects to accurately capture the thermal evolution of the excitonic diffusion and recombination process. Specifically, photonic effects (reabsorption, recycling or lateral waveguiding effects[24–26]) will be negligible in both the vertical and lateral directions and phonon-mediated phases transitions are forbidden in such thin flakes[27].

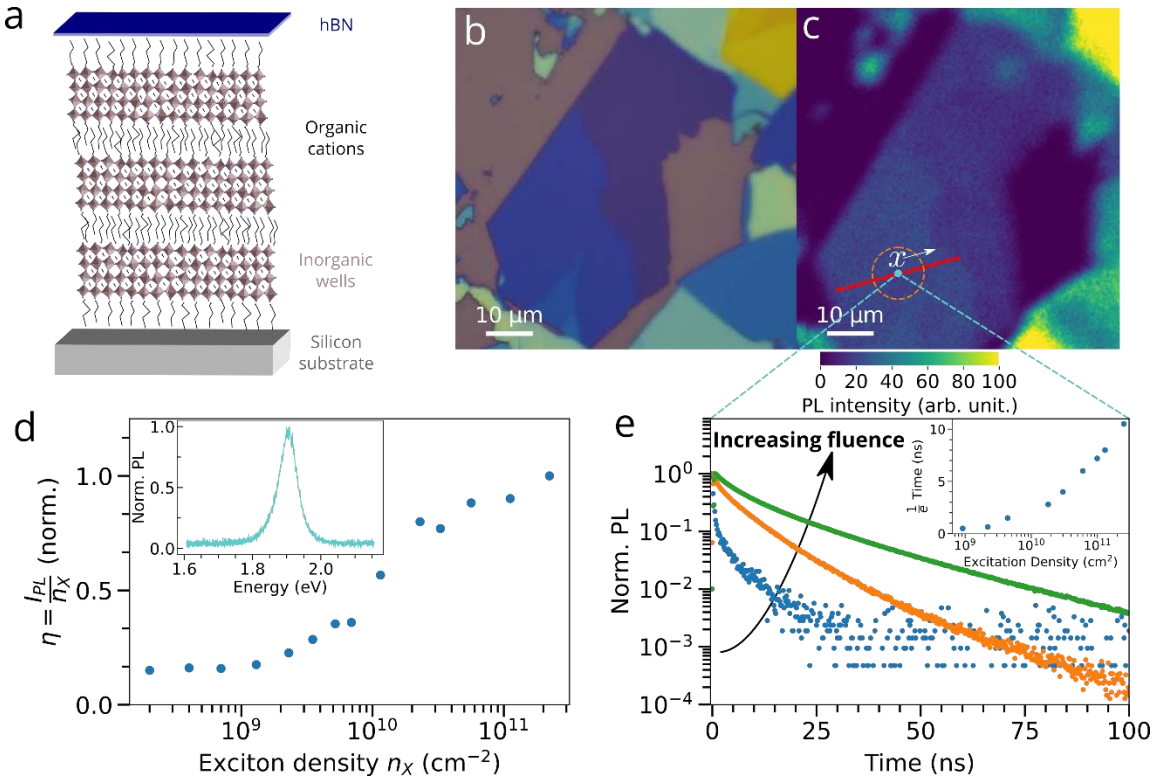

Figure 1: Local photoluminescence properties of the studied $BA_2MA_3Pb_4I_{13}$ $n = 4$ RRP flake at room temperature. (a) Schematic representation of a few layers $n = 4$ RRP flake. (b) Optical reflection and (c) PL intensity (excitation at 510 nm) images. The red strip in c highlights the

region of interest over which transport is subsequently analysed, with the spatial parameter x defined spanning from the centre of the region. (d) Evolution of the normalised PL efficiency η as a function of injected exciton density, n_x, with η defined as the ratio of the number of emitted photons (PL intensity, I_{PL}) to the number of injected excitons n_x, arbitrarily normalised to 1 for clarity. Inset, the normalised PL spectrum at the same location. (e) Time-resolved PL decays for increasing injected exciton densities at the centre of the region of interest highlighted on c, with exciton density increasing between 9.2×10^8 cm^{-2} (blue), 3.0×10^{10} cm^{-2} (orange) and 2.5×10^{11} cm^{-2} (green) for emitted wavelengths shorter than ~ 800 nm. Inset $\frac{1}{e}$ times for TRPL decays as a function of excitation density.

Figure 1c displays the photoluminescence (PL) intensity map of the flake of interest. The local PL spectrum of this flake (Figure 1d inset) is centred at ≈ 1.9 eV, as expected for a high-quality pure phase n = 4 flake[16], suggesting no other n phases are present in that region (see SI Section VIII, Figure S4 and Table S1). We first measure the local PL properties in the region of interest (Figure 1c) at different excitation regimes with a 510 nm pulsed laser diode (see SI Section IX for details and Figures S5 - S6 for further data). In Figure 1d, we show the PL intensity as a function of excitation density n_x, weighted by the excitation density n_x, to provide a relative PL efficiency, η (i.e. normalised number of emitted photons per injected exciton; see SI Section X for further data and Figure S7 for absolute PL intensity). We observe that this curve forms an S-shape comprised of two plateaus separated by a growth phase, which can be ascribed to different regimes of trap state filling[28]. Below $n_x \approx 2 \times 10^9$ cm^{-2} the relative PL efficiency remains constant, indicating that the trap filling process is inefficient in this range of exciton densities. This is explained by the fact that the concentration of available traps remains much larger than that of injected excitons across this excitation regime. Above this n_x value, η rises significantly as the PL intensity increases superlinearly with respect to the exciton density. Across this regime, the exciton density is large enough to fill a non-negligible proportion of traps[7], leading to an increase of the PL efficiency. This trap filling occurs up to a saturation of this effect at $n_x \approx 3 \times 10^{10}$ cm^{-2}, above which η

again remains constant with increasing excitation density and a large proportion of excitons are recombining radiatively. Similar observations can be made when considering time-resolved PL (TRPL) decays as a function of the exciton density (Figures 1e, 1e inset, S8 and S9). In the low exciton density regime (9.2×10^8 cm^{-2}, blue data) corresponding to the first plateau, the TRPL curve exhibits a rapid decay, with a PL lifetime of 0.5 ns defined as the time to fall to $\frac{1}{e}$ of the initial intensity[23], consistent with fast non-radiative decay of trapped excitons as the primary recombination channel. Above this first plateau, the TRPL lifetime increases with increasing excitation density (3.0×10^{10} cm^{-2}, orange data), until the second plateau is reached (Figures 1e inset and S9). At this second plateau (2.50×10^{11} cm^{-2}, green data), we observe a quasi mono-exponential decay with a $\frac{1}{e}$ PL lifetime of ≈ 11 ns, which is consistent with classical first order exciton recombination kinetics dominated by a radiative rate that is outcompeting the non-radiative rate.[7]

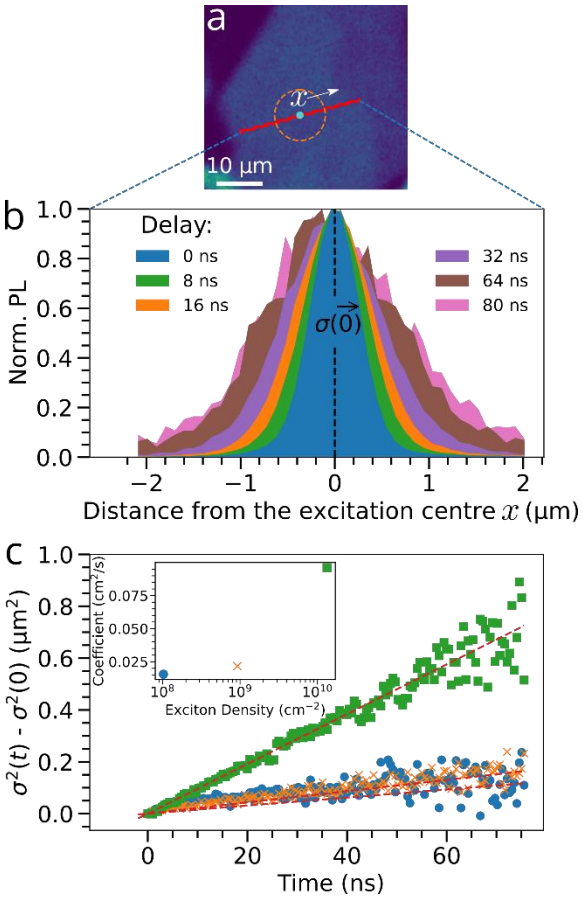

Figure 2: Local spatially resolved diffusion measurements in a $BA_2MA_3Pb_4I_{13}$ (n = 4) RRP flake at different fluences. (a) PL map highlighting the region of interest. (b) Selected spatial PL profiles, normalised, at different times after excitation by the laser pulse, localised at x = 0 (centre of the red line in Figure 2a). (c) Spreading profiles showing the temporal evolution of the squared broadening quantities $\sigma^2(t) - \sigma^2(0)$ of the spatial profiles for the flake at room temperature on the region of interest at three different densities of injected excitons. Inset: Diffusion coefficients extracted from fits to the data with Equation 1. To clearly visualise the spreading effect, the profiles shown in (b) were obtained with a 0.8 NA 100 x objective lens (generating a narrower initial exciton distribution), whereas all other data throughout, including the in panel c, were taken with a 0.4 NA 10x objective lens which is more suitable for the cryogenic measurements and does not alter the diffusion measurements (see SI Section XI and Figure S10).

We now use the same TRPL microscope setup to investigate the impact of this trap filling process on exciton transport. In this configuration, the sample is excited in the same local region at time t = 0 at a fixed position (x = 0) with a Gaussian shaped laser pulse (cf. blue circle Figure 1c), with the PL subsequently collected as a function of time (t) at different spatial points (x) away from the

excitation spot (see Figure S1 for setup). The resulting spectrally integrated spatial PL profiles, from the region highlighted in Figure 2a, are displayed as a function of time in Figure 2b in the low excitation density regime ($n_x \approx 1.0 \times 10^8$ cm^{-2}), with the increase in the standard deviation of the Gaussian spread $\sigma(t)$ with time consistent with excited species spreading laterally after excitation (see SI Section XII and Figures S11 and S12 for Gaussian profiles and fits at selected times). We find a linear relationship between the quantity $[\sigma^2(t) - \sigma^2(0)]$ and t (Figure 2c), indicating that the spatial broadening is due to classical exciton diffusion[23,29], and can be related to the exciton diffusion coefficient D using the formula [23,29,30]:

$$\sigma^2(t) - \sigma^2(0) = 2Dt \qquad (1).$$

Linear fits to the data in Figure 2c with Equation (1) yields a diffusion coefficient of 0.018 cm^{-2}s^{-1} for $n_x = 1.0 \times 10^8$ cm^{-2} (Figure 2c inset). At this low exciton density, we expect exciton trapping to dominate based on the earlier PL efficiencies, η. At higher exciton densities corresponding to the beginning of the trap saturation regime ($n_x = 9.2 \times 10^8$ cm^{-2}), the fitted diffusion coefficient increased slightly to 0.021 cm^{-2}s^{-1}, and then increases significantly to 0.096 cm^{-2}s^{-1} at even higher exciton densities ($n_x = 1.3 \times 10^{10}$ cm^{-2}) in which a large proportion of the traps are saturated. We note that there is no significant deviation from the linear evolution of $[\sigma^2(t) - \sigma^2(0)]$ across these excitation densities across the accessible time scales, suggesting that non-linear effects such as exciton-exciton annihilation are not influencing the exciton dynamics. These measurements reveal that the local trap states not only limit the PL efficiency but also limit exciton diffusion in these RPPs systems, consistent with other 2D semiconductors.[20,31] Similar behaviour is observed for an $n = 2$ sample (see SI Section XIII and Figures S13 - S16).

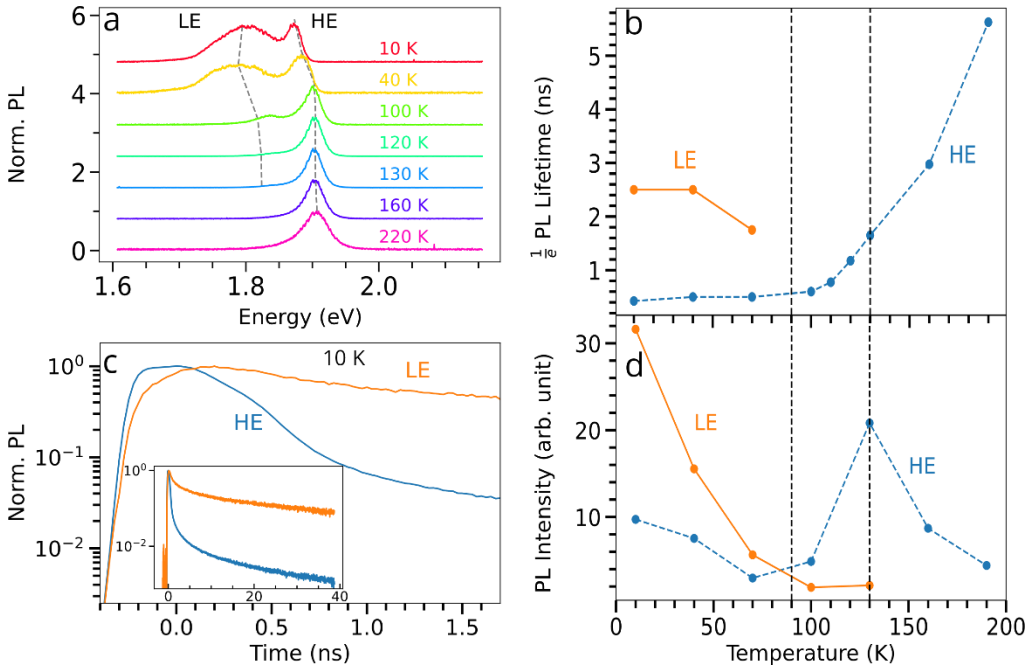

Figure 3: Temperature-dependent PL spectra and exciton dynamics in a $BA_2MA_3Pb_4I_{13}$ RRP flake. Measurements were taken at the centre of region of interest investigated earlier**.** (a) PL spectra showing the evolution of the high energy (HE) peak and the emergence of the low energy (LE) peak at low temperatures, with excitation at 510 nm. Spectra are normalised to the maximum value of each spectrum and vertically offset for clarity. Grey dotted lines tracking the peak centres are guides to the eye. Spectrally selected (b) $\frac{1}{e}$ lifetimes of the LE and high energy (HE) components. (c) Spectrally selected TRPL decays corresponding to the HE and the LE resonance at 10 K, exhibiting the population transfer process. Inset, corresponding decay on the longer time scale. (d) Spectrally selected PL intensities as a function of temperature. Measurements were performed with an excitation density of 9.2×10^8 cm^{-2}. Spectral selection is achieved using appropriate bandpass filters (see SI Section XVI and Figure S22).

To further understand the exciton dynamics and transport, we performed temperature-dependent studies on the same region of the $n = 4$ flake (see SI Section XIV for further PL data). We show local PL spectra in Figure 3a as a function of temperature (see Figure S17 for spectra at other temperatures and Figure S18 for the integrated PL intensity). The position of the main PL resonance, which we refer to herein as the high-energy (HE) peak, does not shift significantly from ≈ 1.9 eV upon decreasing temperature from 300 K to 80 K. This lack of shift is consistent with a strong influence of phonons on the exciton properties[11,32,33] that counterbalance the usual PL

redshift in 3D perovskites attributed to the thermal contraction of the crystal within this temperature range[34,35], rather than other effects such as self-trapped excitons[32]. The redshift behaviour is recovered over the range 120 to 10 K where the contribution of optical phonons should be negligible. Indeed, the lowest optical phonon mode energy in similar systems have been reported to be ≈ 10 meV [35–37], corresponding to threshold temperatures around ≈ 120 K. Further evidence for the influence of phonons on the exciton properties is seen in the decrease of the PL resonance width of the HE peak from ≈ 99 meV at 300 K to 22 meV at 100 K (Figure S19) [32,34].

To further our understanding of the exciton dynamics, we analysed the evolution of the TRPL decays as a function of temperature (see Figure S20 for all decays). The $\frac{1}{e}$ PL lifetime in the HE peak, reduces significantly from ~ 6 ns at 190 K to 2.9 ns at 100 K with an exciton density of 9.2 × 10^8 cm^{-2} (Figure 3b). We note that such relatively short PL lifetimes are to be expected for excitonic semiconductors which possess large oscillator strengths. The general decrease in PL lifetime with decreasing temperature can again, in part, be attributed to a freezing out of phonons, either by the lack of exciton-phonon coupling at low temperatures preventing excitons from escaping local traps states or, by analogy with $MoSe_2$[38] or GaAs quantum wells[39], by a lack of phonons that otherwise push excitons away from the bottom of the band and thus prevent recombination until they return. Interestingly, this decrease in PL lifetime is first accompanied by an increase in PL intensity down to 130 K (Figure 3d), but below 130 K the PL intensity reduces significantly. This drop in PL intensity at ≈ 130 K occurs concomitant with the emergence (Figure 3a) and rapid increase in intensity (Figure 3d) of a second, broader PL resonance at ≈ 1.8 eV, referred to hereafter as the low-energy (LE) resonance. This LE resonance indicates the presence of radiative states situated energetically below the classical excited state continuum. Indeed, LE resonances have been previously reported in 2D perovskites and often attributed either to self-

trapped excitons[40–44] (STE) or defect-assisted emission[45] (DAE). To our knowledge, there is no strong evidence of self-trapped exciton properties in the BA-based RPPs family[46], while such properties are regularly observed in RPP families based on specific organic cations leading to distortions of the perovskite lattice[47]. In addition, the STE PL intensity is often maximal at an intermediary temperature of around 100 K[48], while our LE resonance is maximal at 10 K (see Figure 3a). Finally, we show in Figure S21 (see SI Section XV) that LE resonance saturates at high excitation intensity in comparison to the HE one, which suggests a local and extrinsic emission process rather than an intrinsic process that would occur evenly across the sample and would saturate. We will therefore mostly consider the DAE hypothesis in the following analyses and simulations. Nevertheless, many of our observations would also be compatible with a hybrid (STE/DAE) situation that has been reported recently[43] in which the STE effects is heterogeneously triggered across the sample due to the presence of extrinsic local features. Based on the literature[40–44], and our spectroscopic measurements including the ability to saturate the states, we do not believe that the LE states result from a phase change within the material..Unambiguous assignment of the precise nature of the LE states will require further studies that are beyond the scope of the present work.

In many lead halide perovskites materials, the LE emission has been associated with local impurity phases such as excess iodine precursors[45,49], and is generally only readily apparent at low temperature[44,45,50,51]. We note that the nature of these localised radiative states appears to be distinct from the non-radiative trap states discussed above, consistent with a general rise of the total PL intensity (LE + HE) observed between 200 K and 10 K (Figure 3d and Figure S18). We cannot definitively rule out the presence of the LE states above 100 K, however if the LE states

are present their impact should be negligible, as attested to by the PL spectra showing only minor tails in the LE region above 100 K (Figures 3a and S17). .

The decrease in intensity of the HE peak together with the rise in intensity of the LE peak at low temperature hints at a transfer of exciton population from the HE to LE states[16], and we will herein refer to this as downhill energy transfer. This transfer effect is evident by considering the spectrally resolved PL dynamics, achieved using appropriate bandpass filters (see SI Section XVI and Figure S22), at a given temperature, exemplified in Figure 3c at 10 K (see SI Section XVII and Figure S23 for other temperatures). Within the first nanosecond after the excitation pulse, we observe both a fast decline of the HE component and a rise of the LE component with a rise time of ≈ 0.5 ns (time between the maximum of the HE component and the maximum of the LE component), longer than the setup instrument response of ≈ 385 ps (see SI Section XVIII and Figure S24). After another few hundred picoseconds, the LE component starts declining but at a reduced rate compared to the HE signal. The PL decay of the LE component extends over ≈ 40 ns (Figure 3c), suggesting that once the excitons reach these LE states, their recombination is slower than in the HE states.

We now consider the temperature-dependent transport properties, and the impact of this energy transfer process on these properties. We start by analysing the diffusion properties associated with the HE peak as a function of temperature at a low exciton density of $n_x = 9.2 \times 10^8$ cm^{-2}. We limit our measurements to temperatures below 200 K to maintain a low pressure without disturbing the measurements with the vibrating vacuum cryopump (see SI Sections II, III and IV). We find that the diffusion coefficient decreases significantly from 0.03 cm^2.s^{-1} at 200 K to a negligible value (< 0.001 cm^2.s^{-1}) below 100 K (see Figures 4c and an example fit at 160 K in Figure 4b; see SI Section XIX and Figures S25 - S28 for Gaussian profiles and resulting spreading curves at

different temperatures). This suggests that the excitons are progressively less likely to transfer through the HE sites with decreasing temperature. We note that PL spectra from the studied region, taken before and after each diffusion measurement, show no appreciable change in the HE resonance at any temperature and only small shifts in the LE resonance at 100 K and 130 K, ruling out structural changes or laser induced damage occurring during the measurements and influencing the results (see SI Section XX and Figure S29).

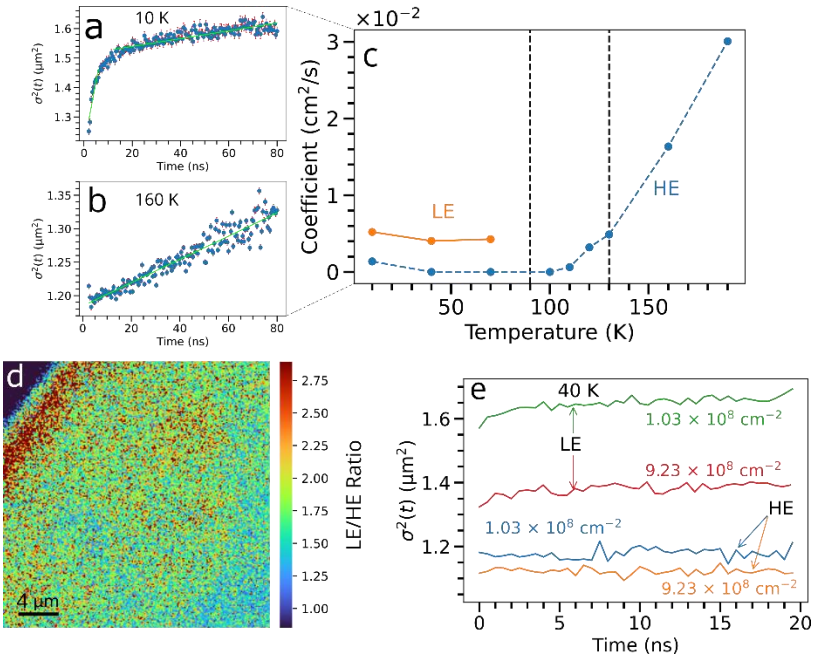

Figure 4: Temperature-dependent transport properties in a $BA_2MA_3Pb_4I_{13}$ RRP flake. Spreading profiles at (a) 10 K and (b) 160 K with an excitation density of 9.2×10^8 cm^{-2}. (c) Effective spreading coefficients extracted from fitting the underlying spreading profiles to Equation 1, exemplified by the linear fits in green in a and b, Figures S26 and S28. For the LE components only the initial fast spreading coefficients are shown. (d) Ratio of normalised confocal PL maps at 10 K with excitation at 510 nm of the flake allowing the distinction of the regions containing LE and HE peaks, obtained using bandpass filters. (e) Spreading profiles at 40 K for different injected exciton densities with LE and HE peaks distinguished using the bandpass filters (see SI Section XVI and Figure S22).

To consider the transport associated with the LE and HE sites, we show in Figure 4d a map, which is a ratio of PL maps taken using appropriate bandpass filters (see SI Section XVI and Figure S22),

of the region of interest at 10 K, showing a spatial distribution of these LE and HE sites. Fluence-dependent measurements show that the emission from the LE states saturate when the excitation density is of the order of $\approx 9 \times 10^8$ cm^{-2} (Figure S21), indicating that a significant portion of the created excitons would have been unable to access these LE states. This is likely due to a lower concentration of LE regions across the flake, together with slower recombination, compared to the HE regions. This result shows that the spatial energy landscape is comprised of many HE-only domains, sparsely interspersed with LE subdomains. As these LE and HE states are dispersed across the sample, we now consider whether such an exciton transfer system observed can promote a lateral motion of the excitons beyond the classical diffusive process. We show the extracted exciton transport coefficient corresponding to the LE and HE peaks in Figure 4c, again at a low exciton density of 9.2×10^8 cm^{-2} (see Figure 4a for an example of the spreading observed for the LE peak at 10 K). A very slow spatial spreading of the PL profile is observed for the HE resonance, comparable to the diffusion coefficient measured just above 100 K. However, the LE band exhibits an initial fast spreading of the spatial PL profile, on the order of a nanosecond, followed by a regime over the next ≈ 80 ns during which negligible spreading occurs. Further fluence-dependent measurements (Figure 4e) reveal that the transport contribution associated with the LE bands saturates at higher exciton density, consistent with the saturation of the PL from these states. These observations indicate that an efficient lateral motion of the excitons occurs with the same nanosecond timescale as the HE-to-LE population transfer discussed earlier. We propose that the two effects are connected and that the large energy gradient between adjacent HE and LE regions causes excitons to rapidly drift toward the LE states, dispersed throughout the flake, through the downhill energy transfer mechanism introduced earlier (Figure 5b). With this in mind, we propose that D the diffusion coefficient be re-termed as the spreading coefficient (cm^{-2}/s), to account for

the fact that diffusion is not the only transport mechanism that will affect the rate of spreading of the PL profile (Figure 4c).

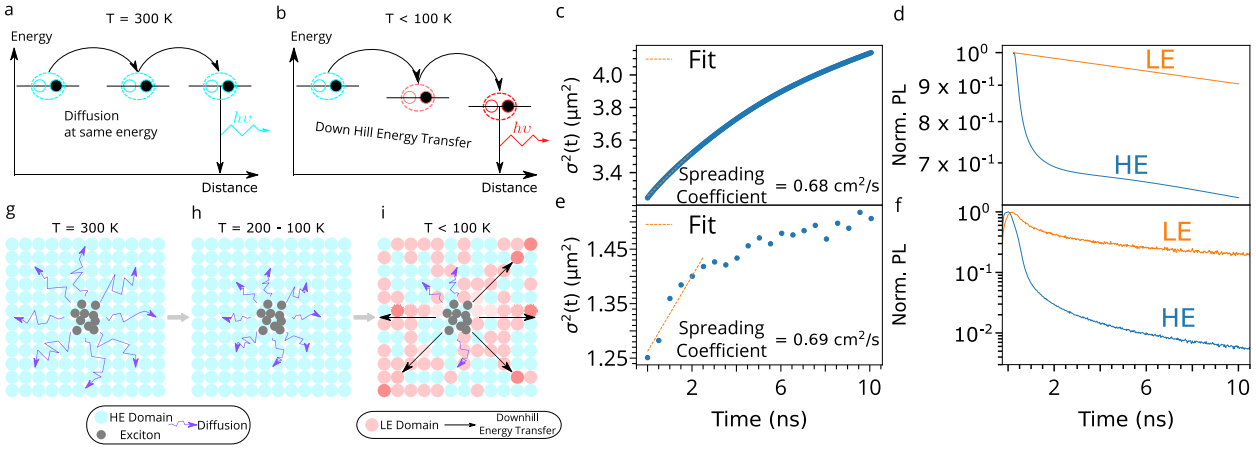

Figure 5: Understanding energy transfer mechanisms in a $BA_2MA_3Pb_4I_{13}$ RRP flake at varying temperatures. (a) At room temperature diffusion mediated by thermally activated hopping processes is the dominant exciton transport mechanism. (b) Downhill energy transfer transport to lower energy sites at lower temperature. Modelled (c) spreading curve and (d) log scaled TRPL decays. Experimental (e) spreading curve and (f) TRPL decays from the actual flake at an exciton density of 9.2×10^8 cm^{-2}. (g) – (i) Schematics to represent the proposed transport model over the studied temperature ranges. (g) Dominant diffusive transport, at room temperature. (h) As the temperature is lowered the diffusion process becomes less efficient. (i) At T < 100 K, the LE states emerge, and downhill energy transfer becomes the dominant transport mechanism. The lengths of the diffusion and downhill energy transfer indicators are indicative of the rates of these processes. Outputs from simulations of our proposed model, Equation 2, compared to experiment, see SI Section XXI for parameters used.

To validate these interpretations, we model the impact of the LE and HE domains on the exciton transport in this low temperature regime. This simulation uses a finite element approach to solve the corresponding 2D drift-diffusion equation to describe how the local exciton density $n(\vec{r},t)$ evolves in time t and space $\vec{r}$:

$$\frac{\partial n(\vec{r},t)}{\partial t} = -kn(\vec{r},t) + D\nabla^2 n(\vec{r},t) + \mu\nabla\left(n(\vec{r},t)\nabla u(\vec{r})\right) \qquad (2)$$

where the first term on the right-hand side corresponds to exciton recombination, k is the recombination rate constant, and the second term to exciton diffusion, D the diffusion coefficient. The third term accounts for the drift of excitons inside the energy gradient, with μ being the exciton mobility and $u(\vec{r})$ the local energetic potential felt by an exciton located at position $\vec{r}$. We fixed the value of several parameters to our experimental results at 10 K (see SI Section XXI for details): specifically, we use distinct exciton recombination rates extracted from TRPL decays (Figure 5f) for the HE and the LE domains of k_{HE} = 0.6 ns^{-1} and k_{LE} = 0.01 ns^{-1}, with $k = k_{HE} + k_{LE}$. Furthermore, we model the energy landscape of the sample at 10 K as being composed of adjacent domains of both HE (energy range 1.85 – 1.91 eV) and LE (broader energy range of 1.60 – 1.85 eV) using the spatial distribution from the PL maps in Figure 4d and the PL spectra in Figure 3a. Thus, D is the only adjusted parameter. The finite difference mesh employed to solve the equation consists of a 256 x 256 grid, resulting in individual domain sizes equivalent to 80 nm. Using these conditions, we simulated the spatiotemporal evolution of the excitons at 10 K (Figures 5c and 5d) and qualitatively reproduced the main features of the dynamics, in particular the fast spreading of the exciton distribution with spreading coefficient D = 0.68 $cm^2.s^{-1}$ (Figure 5c; see SI Section XXI and Figure S30 for other simulations) closely matching the experimental value of 0.69 $cm^2.s^{-1}$ (Figure 5e). We highlight here that a fully quantitative agreement is beyond the scope of this study as it would require a quantitative evaluation of the local concentration and energy of LE States with a nanoscale resolution that cannot be reached with optical microscopy. Nevertheless, the results from this model validate our understanding of the observations in which the local energy gradient drives the excitons to move downward in energy, which results in a lateral movement of excitons from the HE to the LE domains. The fact that LE sites can saturate allows exploration of

further LE sites, leading to long-distance energy transport (up to ≈ 600 nm) through this downhill energy transfer effect.

Based on our collective results, we propose a general description of the exciton dynamics in these RPP flakes that is summarised in Figures 5a – 5b and 5g – 5i. At room temperature and down to ≈ 100 K, exciton transport is governed by an interplay between non-radiative trap states and phonons. In this picture (Figures 5a and 5g), exciton diffusion occurs via a hopping process in which significant thermal energy provided by phonons is required to promote excitons from localised states toward the excited state continuum. Such a diffusion process is efficient at high temperatures, though this also means that excitons can more readily find deep trap states on which they recombine non-radiatively; hence the PL efficiency generally increases with decreasing temperature. Diffusion becomes less efficient at lower temperature as fewer phonons states are populated (Figure 5h) and, at or below 100 K, the exciton-phonon coupling effects freeze out due to a negligible population of optical phonons[11,36,37] in such RPP flakes. At ≈ 130 K, a series of broad, lower energy (LE) states are detectable, connected to the heterogeneous static disorder in the material. At temperatures below 100 K, excitons are split into two populations: one which is localised before recombining, leading to the HE resonance. In parallel, a fraction of these excitons moves laterally as they transfer down into the LE sites (Figures 5b and 5i). Remarkably, this downhill energy transfer process recovers long-range exciton transport (≈ 600 nm) at low temperature despite the absence of phonon population.

We have shown here that the exciton dynamics in these RPP flakes are highly tuneable and could be exploited to design tailored optoelectronics devices. For example, one could tune the transport length of excited species over several orders of magnitude by implementing a controlled design of the spatial distribution of the LE states via chemical routes[50,51]. Furthermore, the saturation of the

LE sites means that an external operator could be used to turn their properties on and off at will, for instance by modulating the exciton density through illumination intensity or injection rate. This effect opens the possibility of light emitting devices in which the dominant emission wavelength can be selectively tuned. Finally, as these LE states are connected to the static disorder and the phononic properties of these flakes, one could design mechanical and/or vibrational[52] strategies to modulate them in optomechanic device architectures[52,53].

In conclusion, we studied the local temperature-dependent dynamics and transport of excitons in thin Ruddlesden-Popper perovskite flakes using time-resolved luminescence microscopy. We identified the existence of several temperature regimes and highlighted the interplay between excitons, phonons, and the local energetic landscape. Below 100 K, the exciton diffusion process is inefficient due to the absence of optical phonons. Yet, we showed that excitons can still travel through a static disorder landscape scheme in which long-lived radiative shallow states play an important role. At higher temperatures, the progressive population of the phonon modes causes dynamic disorder to dominate over static disorder. In parallel, the exciton-phonon coupling allows the exciton to move across the crystal in a diffusive fashion, hopping from one shallow trap to the next until they either recombine radiatively or they encounter non-radiative deep trap states. Phonons induce dynamic disorder, increasing the exciton mobility, enabling the excitons to reach non-radiative deep traps. This study provides new microscopic visualisation of the fundamental mechanisms underlying the exciton dynamics in these RPP flakes, and highlights the major role played by the energetic landscape in the diffusion process in such 2D materials. With fine control over such a landscape, and in particular the presence of non-radiative deep traps states, we could control the efficiency of the excitonic motion and design highly efficient optoelectronics devices

based on these Ruddlesden-Popper perovskites. Further work will be required to understand the nature of the low-energy states to allow facile material control over the formation and distributions.

ASSOCIATED CONTENT

Supporting Information. Details on the sample preparation, the microscopy PL and cryogenics setup, additional photoluminescence characterization of the samples (spectrally and time resolved data). Diffusion measurements at different temperatures. Complementary results on n = 2 RPP crystals. Low temperature spectral and temporal study of n = 4 crystals. Further details of the simulations.

The following files are available free of charge.

AUTHOR INFORMATION

[§] A.B and G.D contributed equally.

ACKNOWLEDGMENT

The authors acknowledge the European Research Council (ERC) under the European Union's Horizon 2020 research and innovation program (HYPERION, Grant Agreement Number 756962). SDS acknowledges funding from the Royal Society and Tata Group (UF150033). GD acknowledges the Royal Society for funding through a Newton International Fellowship. GD and SDS acknowledge the UK Engineering and Physical Sciences Research Council (EPSRC) under grant reference EP/R023980/1. A.B. acknowledges a Robert Gardiner Scholarship and funding from Christ's College, Cambridge. K.G. acknowledges support from the Polish Ministry of Science and Higher Education within the Mobilnosc Plus program (GrantNo.

1603/MOB/V/2017/0). The authors thank Niall Goulding and Rachel Bothwell for valuable discussions.

REFERENCES

(1) Stoumpos, C. C.; Kanatzidis, M. G. The Renaissance of Halide Perovskites and Their Evolution as Emerging Semiconductors. *Acc. Chem. Res.* **2015**, *48* (10), 2791–2802. DOI: 10.1021/acs.accounts.5b00229.

(2) Mao, L.; Stoumpos, C. C.; Kanatzidis, M. G. Two-Dimensional Hybrid Halide Perovskites: Principles and Promises. *J. Am. Chem. Soc.* **2019**, *141* (3), 1171–1190. DOI: 10.1021/jacs.8b10851.

(3) Ruggeri, E.; Anaya, M.; Gałkowski, K.; Delport, G.; Kosasih, F. U.; Abfalterer, A.; Mackowski, S.; Ducati, C.; Stranks, S. D. Controlling the Growth Kinetics and Optoelectronic Properties of 2D/3D Lead–Tin Perovskite Heterojunctions. *Adv. Mater.* **2019**, *31* (51), 1905247. DOI: 10.1002/adma.201905247.

(4) Grancini, G.; Roldán-Carmona, C.; Zimmermann, I.; Mosconi, E.; Lee, X.; Martineau, D.; Narbey, S.; Oswald, F.; De Angelis, F.; Graetzel, M.; Nazeeruddin, M. K. One-Year Stable Perovskite Solar Cells by 2D/3D Interface Engineering. *Nat. Commun.* **2017**, *8* (1), 15684. DOI: 10.1038/ncomms15684.

(5) Ishihara, T.; Takahashi, J.; Goto, T. Exciton State in Two-Dimensional Perovskite Semiconductor (C10H21NH3)2PbI4. *Solid State Commun.* **1989**, *69* (9), 933–936. DOI: 10.1016/0038-1098(89)90935-6.

(6) Leng, K.; Fu, W.; Liu, Y.; Chhowalla, M.; Loh, K. P. From Bulk to Molecularly Thin Hybrid Perovskites. *Nat. Rev. Mater.* **2020**, *5* (7), 482–500. DOI: 10.1038/s41578-020-

0185-1.

(7) Delport, G.; Chehade, G.; Lédée, F.; Diab, H.; Milesi-Brault, C.; Trippé-Allard, G.; Even, J.; Lauret, J.-S.; Deleporte, E.; Garrot, D. Exciton-Exciton Annihilation in Two-Dimensional Halide Perovskites at Room Temperature. *J. Phys. Chem. Lett.* **2019**, *10* (17), 5153–5159. DOI: 10.1021/acs.jpclett.9b01595.

(8) Novoselov, K. S. Electric Field Effect in Atomically Thin Carbon Films. *Science (80-.).* **2004**, *306* (5696), 666–669. DOI: 10.1126/science.1102896.

(9) Leng, K.; Abdelwahab, I.; Verzhbitskiy, I.; Telychko, M.; Chu, L.; Fu, W.; Chi, X.; Guo, N.; Chen, Z.; Chen, Z.; Zhang, C.; Xu, Q.-H.; Lu, J.; Chhowalla, M.; Eda, G.; Loh, K. P. Molecularly Thin Two-Dimensional Hybrid Perovskites with Tunable Optoelectronic Properties Due to Reversible Surface Relaxation. *Nat. Mater.* **2018**, *17* (10), 908–914. DOI: 10.1038/s41563-018-0164-8.

(10) Blancon, J.-C.; Stier, A. V.; Tsai, H.; Nie, W.; Stoumpos, C. C.; Traoré, B.; Pedesseau, L.; Kepenekian, M.; Katsutani, F.; Noe, G. T.; Kono, J.; Tretiak, S.; Crooker, S. A.; Katan, C.; Kanatzidis, M. G.; Crochet, J. J.; Even, J.; Mohite, A. D. Scaling Law for Excitons in 2D Perovskite Quantum Wells. *Nat. Commun.* **2018**, *9* (1), 2254. DOI: 10.1038/s41467-018-04659-x.

(11) Gauthron, K.; Lauret, J.-S.; Doyennette, L.; Lanty, G.; Al Choueiry, A.; Zhang, S. J.; Brehier, A.; Largeau, L.; Mauguin, O.; Bloch, J.; Deleporte, E. Optical Spectroscopy of Two-Dimensional Layered (C6H5C2H4-NH3)2-PbI4 Perovskite. *Opt. Express* **2010**, *18* (6), 5912. DOI: 10.1364/OE.18.005912.

(12) Abdel-Baki, K.; Boitier, F.; Diab, H.; Lanty, G.; Jemli, K.; Lédée, F.; Garrot, D.; Deleporte, E.; Lauret, J. S. Exciton Dynamics and Non-Linearities in Two-Dimensional Hybrid

Organic Perovskites. *J. Appl. Phys.* **2016**, *119* (6), 064301. DOI: 10.1063/1.4941345.

(13) Zhang, H.; Liao, Q.; Wu, Y.; Zhang, Z.; Gao, Q.; Liu, P.; Li, M.; Yao, J.; Fu, H. 2D Ruddlesden-Popper Perovskites Microring Laser Array. *Adv. Mater.* **2018**, *30* (15), 1706186. DOI: 10.1002/adma.201706186.

(14) Xiao, Z.; Kerner, R. A.; Zhao, L.; Tran, N. L.; Lee, K. M.; Koh, T.-W.; Scholes, G. D.; Rand, B. P. Efficient Perovskite Light-Emitting Diodes Featuring Nanometre-Sized Crystallites. *Nat. Photonics* **2017**, *11* (2), 108–115. DOI: 10.1038/nphoton.2016.269.

(15) Tsai, H.; Nie, W.; Blancon, J.; Stoumpos, C. C.; Asadpour, R.; Harutyunyan, B.; Neukirch, A. J.; Verduzco, R.; Crochet, J. J.; Tretiak, S.; Pedesseau, L.; Even, J.; Alam, M. A.; Gupta, G.; Lou, J.; Ajayan, P. M.; Bedzyk, M. J.; Kanatzidis, M. G.; Mohite, A. D. High-Efficiency Two-Dimensional Ruddlesden–Popper Perovskite Solar Cells. *Nature* **2016**, *536* (7616), 312–316. DOI: 10.1038/nature18306.

(16) Blancon, J.-C.; Tsai, H.; Nie, W.; Stoumpos, C. C.; Pedesseau, L.; Katan, C.; Kepenekian, M.; Soe, C. M. M.; Appavoo, K.; Sfeir, M. Y.; Tretiak, S.; Ajayan, P. M.; Kanatzidis, M. G.; Even, J.; Crochet, J. J.; Mohite, A. D. Extremely Efficient Internal Exciton Dissociation through Edge States in Layered 2D Perovskites. *Science (80-.).* **2017**, *355* (6331), 1288–1292. DOI: 10.1126/science.aal4211.

(17) Yuan, M.; Quan, L. N.; Comin, R.; Walters, G.; Sabatini, R.; Voznyy, O.; Hoogland, S.; Zhao, Y.; Beauregard, E. M.; Kanjanaboos, P.; Lu, Z.; Kim, D. H.; Sargent, E. H. Perovskite Energy Funnels for Efficient Light-Emitting Diodes. *Nat. Nanotechnol.* **2016**, *11* (10), 872–877. DOI: 10.1038/nnano.2016.110.

(18) Gan, Z.; Wen, X.; Chen, W.; Zhou, C.; Yang, S.; Cao, G.; Ghiggino, K. P.; Zhang, H.; Jia, B. The Dominant Energy Transport Pathway in Halide Perovskites: Photon Recycling or

Carrier Diffusion? *Adv. Energy Mater.* **2019**, *9* (20), 1900185. DOI: 10.1002/aenm.201900185.

(19) Ziegler, J. D.; Zipfel, J.; Meisinger, B.; Menahem, M.; Zhu, X.; Taniguchi, T.; Watanabe, K.; Yaffe, O.; Egger, D. A.; Chernikov, A. Fast and Anomalous Exciton Diffusion in Two-Dimensional Hybrid Perovskites. *Nano Lett.* **2020**, *20* (9), 6674–6681. DOI: 10.1021/acs.nanolett.0c02472.

(20) Seitz, M.; Magdaleno, A. J.; Alcázar-Cano, N.; Meléndez, M.; Lubbers, T. J.; Walraven, S. W.; Pakdel, S.; Prada, E.; Delgado-Buscalioni, R.; Prins, F. Exciton Diffusion in Two-Dimensional Metal-Halide Perovskites. *Nat. Commun.* **2020**, *11* (1), 2035. DOI: 10.1038/s41467-020-15882-w.

(21) Tian, W.; Zhao, C.; Leng, J.; Cui, R.; Jin, S. Visualizing Carrier Diffusion in Individual Single-Crystal Organolead Halide Perovskite Nanowires and Nanoplates. *J. Am. Chem. Soc.* **2015**, *137* (39), 12458–12461. DOI: 10.1021/jacs.5b08045.

(22) Handloser, K.; Giesbrecht, N.; Bein, T.; Docampo, P.; Handloser, M.; Hartschuh, A. Contactless Visualization of Fast Charge Carrier Diffusion in Hybrid Halide Perovskite Thin Films. *ACS Photonics* **2016**, *3* (2), 255–261. DOI: 10.1021/acsphotonics.5b00562.

(23) Stavrakas, C.; Delport, G.; Zhumekenov, A. A.; Anaya, M.; Chahbazian, R.; Bakr, O. M.; Barnard, E. S.; Stranks, S. D. Visualizing Buried Local Carrier Diffusion in Halide Perovskite Crystals via Two-Photon Microscopy. *ACS Energy Lett.* **2020**, *5*, 117–123. DOI: 10.1021/acsenergylett.9b02244.

(24) Diab, H.; Arnold, C.; Lédée, F.; Trippé-Allard, G.; Delport, G.; Vilar, C.; Bretenaker, F.; Barjon, J.; Lauret, J.-S.; Deleporte, E.; Garrot, D. Impact of Reabsorption on the Emission Spectra and Recombination Dynamics of Hybrid Perovskite Single Crystals. *J. Phys. Chem.*

Lett. **2017**, *8* (13), 2977–2983. DOI: 10.1021/acs.jpclett.7b00998.

(25) Bercegol, A.; Ory, D.; Suchet, D.; Cacovich, S.; Fournier, O.; Rousset, J.; Lombez, L. Quantitative Optical Assessment of Photonic and Electronic Properties in Halide Perovskite. *Nat. Commun.* **2019**, *10* (1), 1586. DOI: 10.1038/s41467-019-09527-w.

(26) Pazos-Outon, L. M.; Szumilo, M.; Lamboll, R.; Richter, J. M.; Crespo-Quesada, M.; Abdi-Jalebi, M.; Beeson, H. J.; Vru ini, M.; Alsari, M.; Snaith, H. J.; Ehrler, B.; Friend, R. H.; Deschler, F. Photon Recycling in Lead Iodide Perovskite Solar Cells. *Science (80-.).* **2016**, *351* (6280), 1430–1433. DOI: 10.1126/science.aaf1168.

(27) Chen, Z.; Wang, Y.; Sun, X.; Xiang, Y.; Hu, Y.; Jiang, J.; Feng, J.; Sun, Y.-Y.; Wang, X.; Wang, G.-C.; Lu, T.-M.; Gao, H.; Wertz, E. A.; Shi, J. Remote Phononic Effects in Epitaxial Ruddlesden–Popper Halide Perovskites. *J. Phys. Chem. Lett.* **2018**, *9* (23), 6676–6682. DOI: 10.1021/acs.jpclett.8b02763.

(28) Walker, A. W.; Heckelmann, S.; Karcher, C.; Höhn, O.; Went, C.; Niemeyer, M.; Bett, A. W.; Lackner, D. Nonradiative Lifetime Extraction Using Power-Dependent Relative Photoluminescence of III-V Semiconductor Double-Heterostructures. *J. Appl. Phys.* **2016**, *119* (15), 155702. DOI: 10.1063/1.4945772.

(29) Delport, G.; Macpherson, S.; Stranks, S. D. Imaging Carrier Transport Properties in Halide Perovskites Using Time-Resolved Optical Microscopy. *Adv. Energy Mater.* **2020**, *10* (26), 1903814. DOI: 10.1002/aenm.201903814.

(30) Akselrod, G. M.; Prins, F.; Poulikakos, L. V; Lee, E. M. Y.; Weidman, M. C.; Mork, A. J.; Willard, A. P.; Bulović, V.; Tisdale, W. A. Subdiffusive Exciton Transport in Quantum Dot Solids. *Nano Lett.* **2014**, *14* (6), 3556–3562. DOI: 10.1021/nl501190s.

(31) Kulig, M.; Zipfel, J.; Nagler, P.; Blanter, S.; Schüller, C.; Korn, T.; Paradiso, N.; Glazov,

M. M.; Chernikov, A. Exciton Diffusion and Halo Effects in Monolayer Semiconductors. *Phys. Rev. Lett.* **2018**, *120* (20), 207401. DOI: 10.1103/PhysRevLett.120.207401.

(32) Wang, S.; Ma, J.; Li, W.; Wang, J.; Wang, H.; Shen, H.; Li, J.; Wang, J.; Luo, H.; Li, D. Temperature-Dependent Band Gap in Two-Dimensional Perovskites: Thermal Expansion Interaction and Electron–Phonon Interaction. *J. Phys. Chem. Lett.* **2019**, *10* (10), 2546–2553. DOI: 10.1021/acs.jpclett.9b01011.

(33) Milot, R. L.; Eperon, G. E.; Snaith, H. J.; Johnston, M. B.; Herz, L. M. Temperature-Dependent Charge-Carrier Dynamics in CH 3 NH 3 PbI 3 Perovskite Thin Films. *Adv. Funct. Mater.* **2015**, *25* (39), 6218–6227. DOI: 10.1002/adfm.201502340.

(34) Diab, H.; Trippé-Allard, G.; Lédée, F.; Jemli, K.; Vilar, C.; Bouchez, G.; Jacques, V. L. R.; Tejeda, A.; Even, J.; Lauret, J.-S.; Deleporte, E.; Garrot, D. Narrow Linewidth Excitonic Emission in Organic–Inorganic Lead Iodide Perovskite Single Crystals. *J. Phys. Chem. Lett.* **2016**, *7* (24), 5093–5100. DOI: 10.1021/acs.jpclett.6b02261.

(35) Wright, A. D.; Verdi, C.; Milot, R. L.; Eperon, G. E.; Pérez-Osorio, M. A.; Snaith, H. J.; Giustino, F.; Johnston, M. B.; Herz, L. M. Electron–Phonon Coupling in Hybrid Lead Halide Perovskites. *Nat. Commun.* **2016**, *7* (1), 11755. DOI: 10.1038/ncomms11755.

(36) Ni, L.; Huynh, U.; Cheminal, A.; Thomas, T. H.; Shivanna, R.; Hinrichsen, T. F.; Ahmad, S.; Sadhanala, A.; Rao, A. Real-Time Observation of Exciton–Phonon Coupling Dynamics in Self-Assembled Hybrid Perovskite Quantum Wells. *ACS Nano* **2017**, *11* (11), 10834–10843. DOI: 10.1021/acsnano.7b03984.

(37) Guo, Z.; Wu, X.; Zhu, T.; Zhu, X.; Huang, L. Electron–Phonon Scattering in Atomically Thin 2D Perovskites. *ACS Nano* **2016**, *10* (11), 9992–9998. DOI: 10.1021/acsnano.6b04265.

(38) Robert, C.; Lagarde, D.; Cadiz, F.; Wang, G.; Lassagne, B.; Amand, T.; Balocchi, A.; Renucci, P.; Tongay, S.; Urbaszek, B.; Marie, X. Exciton Radiative Lifetime in Transition Metal Dichalcogenide Monolayers. *Phys. Rev. B* **2016**, *93* (20), 205423. DOI: 10.1103/PhysRevB.93.205423.

(39) Damen, T. C.; Shah, J.; Oberli, D. Y.; Chemla, D. S.; Cunningham, J. E.; Kuo, J. M. Exciton Dynamics in GaAs Quantum Wells. *J. Lumin.* **1990**, *45* (1–6), 181–185. DOI: 10.1016/0022-2313(90)90139-3.

(40) Hu, T.; Smith, M. D.; Dohner, E. R.; Sher, M.-J.; Wu, X.; Trinh, M. T.; Fisher, A.; Corbett, J.; Zhu, X.-Y.; Karunadasa, H. I.; Lindenberg, A. M. Mechanism for Broadband White-Light Emission from Two-Dimensional (110) Hybrid Perovskites. *J. Phys. Chem. Lett.* **2016**, *7* (12), 2258–2263. DOI: 10.1021/acs.jpclett.6b00793.

(41) Cortecchia, D.; Yin, J.; Bruno, A.; Lo, S.-Z. A.; Gurzadyan, G. G.; Mhaisalkar, S.; Brédas, J.-L.; Soci, C. Polaron Self-Localization in White-Light Emitting Hybrid Perovskites. *J. Mater. Chem. C* **2017**, *5* (11), 2771–2780. DOI: 10.1039/C7TC00366H.

(42) Cortecchia, D.; Neutzner, S.; Yin, J.; Salim, T.; Srimath Kandada, A. R.; Bruno, A.; Lam, Y. M.; Martí-Rujas, J.; Petrozza, A.; Soci, C. Structure-Controlled Optical Thermoresponse in Ruddlesden-Popper Layered Perovskites. *APL Mater.* **2018**, *6* (11), 114207. DOI: 10.1063/1.5045782.

(43) Paritmongkol, W.; Powers, E. R.; Dahod, N. S.; Tisdale, W. A. Two Origins of Broadband Emission in Multilayered 2D Lead Iodide Perovskites. *J. Phys. Chem. Lett.* **2020**, *11* (20), 8565–8572. DOI: 10.1021/acs.jpclett.0c02214.

(44) Wu, X.; Trinh, M. T.; Niesner, D.; Zhu, H.; Norman, Z.; Owen, J. S.; Yaffe, O.; Kudisch, B. J.; Zhu, X.-Y. Trap States in Lead Iodide Perovskites. *J. Am. Chem. Soc.* **2015**, *137* (5),

2089–2096. DOI: 10.1021/ja512833n.

(45) Kahmann, S.; Tekelenburg, E. K.; Duim, H.; Kamminga, M. E.; Loi, M. A. Extrinsic Nature of the Broad Photoluminescence in Lead Iodide-Based Ruddlesden–Popper Perovskites. *Nat. Commun.* **2020**, *11* (1), 2344. DOI: 10.1038/s41467-020-15970-x.

(46) Lin, C.-W.; Liu, F.; Chen, T.-Y.; Lee, K.-H.; Chang, C.-K.; He, Y.; Leung, T. L.; Ng, A. M. C.; Hsu, C.-H.; Popović, J.; Djurišić, A.; Ahn, H. Structure-Dependent Photoluminescence in Low-Dimensional Ethylammonium, Propylammonium, and Butylammonium Lead Iodide Perovskites. *ACS Appl. Mater. Interfaces* **2020**, *12* (4), 5008–5016. DOI: 10.1021/acsami.9b17881.

(47) Mao, L.; Wu, Y.; Stoumpos, C. C.; Wasielewski, M. R.; Kanatzidis, M. G. White-Light Emission and Structural Distortion in New Corrugated Two-Dimensional Lead Bromide Perovskites. *J. Am. Chem. Soc.* **2017**, *139* (14), 5210–5215. DOI: 10.1021/jacs.7b01312.

(48) Yangui, A.; Garrot, D.; Lauret, J. S.; Lusson, A.; Bouchez, G.; Deleporte, E.; Pillet, S.; Bendeif, E. E.; Castro, M.; Triki, S.; Abid, Y.; Boukheddaden, K. Optical Investigation of Broadband White-Light Emission in Self-Assembled Organic–Inorganic Perovskite (C 6 H 11 NH 3) 2 PbBr 4. *J. Phys. Chem. C* **2015**, *119* (41), 23638–23647. DOI: 10.1021/acs.jpcc.5b06211.

(49) Zhang, Q.; Ji, Y.; Chen, Z.; Vella, D.; Wang, X.; Xu, Q.-H.; Li, Y.; Eda, G. Controlled Aqueous Synthesis of 2D Hybrid Perovskites with Bright Room-Temperature Long-Lived Luminescence. *J. Phys. Chem. Lett.* **2019**, *10* (11), 2869–2873. DOI: 10.1021/acs.jpclett.9b00934.

(50) Booker, E. P.; Thomas, T. H.; Quarti, C.; Stanton, M. R.; Dashwood, C. D.; Gillett, A. J.; Richter, J. M.; Pearson, A. J.; Davis, N. J. L. K.; Sirringhaus, H.; Price, M. B.; Greenham,

N. C.; Beljonne, D.; Dutton, S. E.; Deschler, F. Formation of Long-Lived Color Centers for Broadband Visible Light Emission in Low-Dimensional Layered Perovskites. *J. Am. Chem. Soc.* **2017**, *139* (51), 18632–18639. DOI: 10.1021/jacs.7b10223.

(51) Baranowski, M.; Urban, J. M.; Zhang, N.; Surrente, A.; Maude, D. K.; Andaji-Garmaroudi, Z.; Stranks, S. D.; Plochocka, P. Static and Dynamic Disorder in Triple-Cation Hybrid Perovskites. *J. Phys. Chem. C* **2018**, *122* (30), 17473–17480. DOI: 10.1021/acs.jpcc.8b05222.

(52) Shu, L.; Ke, S.; Fei, L.; Huang, W.; Wang, Z.; Gong, J.; Jiang, X.; Wang, L.; Li, F.; Lei, S.; Rao, Z.; Zhou, Y.; Zheng, R.-K.; Yao, X.; Wang, Y.; Stengel, M.; Catalan, G. Photoflexoelectric Effect in Halide Perovskites. *Nat. Mater.* **2020**, *19* (6), 605–609. DOI: 10.1038/s41563-020-0659-y.

(53) Wei, W.; Dai, Y.; Huang, B. Straintronics in Two-Dimensional in-Plane Heterostructures of Transition-Metal Dichalcogenides. *Phys. Chem. Chem. Phys.* **2017**, *19* (1), 663–672. DOI: 10.1039/C6CP07823K.